# Flow Separation Control by a Concave Bump

Jens Lunte<sup>†</sup> and Erich Schülein

Department of High Speed Configurations, Institute of Aerodynamics and Flow Technology,

German Aerospace Center (DLR), 37073 Göttingen, Germany

jens.lunte@dlr.de · erich.schuelein@dlr.de

<sup>†</sup>Corresponding author

#### **Abstract**

The concave bump concept is a passive flow control element to optimize impinging shock-wave/boundary-layer interactions (SWBLI) to a separation free interaction. The concept has been validated experimentally using two canonical wind tunnel models: a two-dimensional (2D) planar model and a 2D axisymmetric model. These models were tested at two Mach numbers and for various shock impingement locations. At the design point the shadowgrams of the flow demonstrated that the bump could suppress the flow separation and the experimental wall pressure distribution matches the theoretically expected shape. Accompanying computational fluid dynamics (CFD) simulations using the DLR TAU code could be validated by the experimental data and attest an improved total pressure recovery. The concept is also applied to a more realistic inlet configuration, a truncated 2D Prandtl-Meyer inlet, where it enables larger total contraction ratios and higher maximum combustion chamber pressures, leading to an increased overall efficiency of the inlet. The findings of this study demonstrate the potential of the concave bump concept for improving the performance of supersonic inlets.

#### 1. Introduction

The flow around a supersonic flight vehicle is characterized by shock-wave/boundary-layer interactions (SWBLI), which occur at the different components of the vehicle. In air intakes with internal compression, the compression process involves a series of oblique shocks that are reflected at the duct walls, leading to SWBLI. Severe SWBLI result in flow separation, which significantly impacts the maximum mass flow rate and overall pressure recovery of the inlet. In extreme situations the maximum possible contraction of the inlet is reached and the flow can become irreversibly blocked. One critical interaction in this series of SWBLI typically occurs when the initial cowl shock impinges on the boundary layer and dominates the flow behaviour. To mitigate the detrimental behaviour of the cowl shock induced separation, a venting systems are the cowl shock impingement location is usually integrated. However, these venting systems have significant drawbacks, including reduced mass flow through the inlet, increased drag, and the need for more complex thermal protection designs to accommodate the hot air flowing through the vehicle's internal ducts.

An alternative approach, proposed by Schülein et al., 9 to mitigate the detrimental effects of the cowl shock induced SWBLI is the use of a concave bump as a passive flow control element to modify the SWBLI and prevent flow separation. Passive flow control mechanisms are highly desirable due to their simplicity, low maintenance and they require no energy. Figure 1 shows the general shape of the concave bump with the wave system and the expected wall pressure distribution compared to the pressure distribution with separation. In an uncontrolled case, shock-induced separation may occur when the adverse pressure gradient, caused by the reflection of an impinging shock wave, exceeds the boundary layer flow capacity. This forces the flow at the wall to move backwards locally. While the pressure rise over the SWBLI is unavoidable, the concave bump is designed to distribute the pressure rise over a longer distance, so that the boundary layer can handle the pressure gradient at any point without separation. The first half of the pressure rise happens at the windward side of the bump by isentropic compression waves. The expansion at the crest of the bump is crucial to compensate for the pressure jump of the impinging shock, ensuring a smooth increase of the wall pressure. On the leeward side of the bump, the remaining half of the pressure rise due to the SWBLI is generated by another set of isentropic compression waves, which realign the flow with the initial direction. By optimizing the flow with the concave bump, the pressure rise is smooth and gradual, with a pressure gradient that is too shallow to cause boundary layer separation.

The concave bump concept was previously investigated by Schülein et al.<sup>9</sup> on 2D-planar impinging SWBLI, where experimental shadowgrams demonstrated the successful suppression of the separation bubble if the shock hits the design point of the bump. However, the wind tunnel models were only equipped with two wall pressure probes

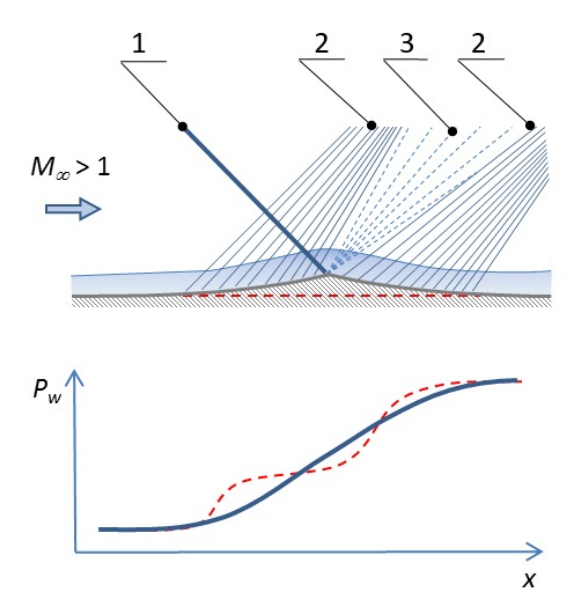


Figure 1: Flow topology and wall-pressure distribution with the concave bump. 1 - impinging shock; 2 - compression waves; 3 - expansion waves

around the immediate vicinity of the crest, which precluded a comprehensive validation of the expected wall pressure distribution. The present paper continues with the validation of the predicted wall pressure distribution by adding additional wall pressure taps to the existing model. Furthermore, the application of the concave bump on axisymmetric configurations was experimentally investigated using a new wind tunnel model. The accompanying computational fluid dynamics (CFD) simulations, conducted with the DLR TAU code, are utilized to quantify the performance gains achieved through the use of the concave bump. Finally, an exploratory parameter study is conducted on 2D truncated Prandtl-Meyer inlets to numerically demonstrate the effectiveness and benefits of the concave bump for inlet applications.

# 2. Experimental Program

## 2.1 Wind tunnel facility

The Ludwieg-Tube Facility RWG at DLR Göttingen<sup>8</sup> (Fig. 2) was choosen for the experimental measurements of this study. The facility has several Laval nozzles to cover a Mach number range of  $2 \le Ma \le 7$  and table 1 summarizes the available freestream unit Reynolds number ( $Re_{1,\infty}$ ) range for the distinct Mach numbers. The Ludwieg tube principle utilizes a pressurised storage tube for the cheap generation of supersonic velocities. The tube is closed at the rear and has a fast opening gate valve that permits a pressure difference towards the adjacent Laval nozzle, measurement section and vacuum tank. When the valve is opened, expansion waves initiate the airflow while travelling towards the closed end of the tube. Flow conditions are quasi stationary until the expansion waves reflect at the end of the tube and return to the entrance of the Laval nozzle. The RWG has two storage tubes with a length of 80 m each, which enables measurement durations between 300 ms and 350 ms, depending on the air temperature in storage tube. Tube B is designed for Mach numbers between 5 and 7. It is heated to prevent the condensation of air components, which would otherwise occur due to the drastic temperature drop in the supersonic nozzle at these Mach numbers. Two windows, each with a clear aperture of  $\emptyset$ 300 mm, are installed on both vertical sides of the Laval nozzle, providing optical access into and through the measurement section. The time-averaged shadowgraph images presented in this paper were captured utilizing a *Cavilux Smart* laser light source in conjunction with a *pco dimax hs4* camera. Table 2 lists all freestream conditions that were investigated during this study.

## 2.2 Test models

Two wind tunnel models, shown in Fig. 3 were investigated in this paper to validate the concave bump concept. The 2D-planar model is an updated version of the model investigated by Schülein et al.<sup>9</sup> The model measures 353 mm in

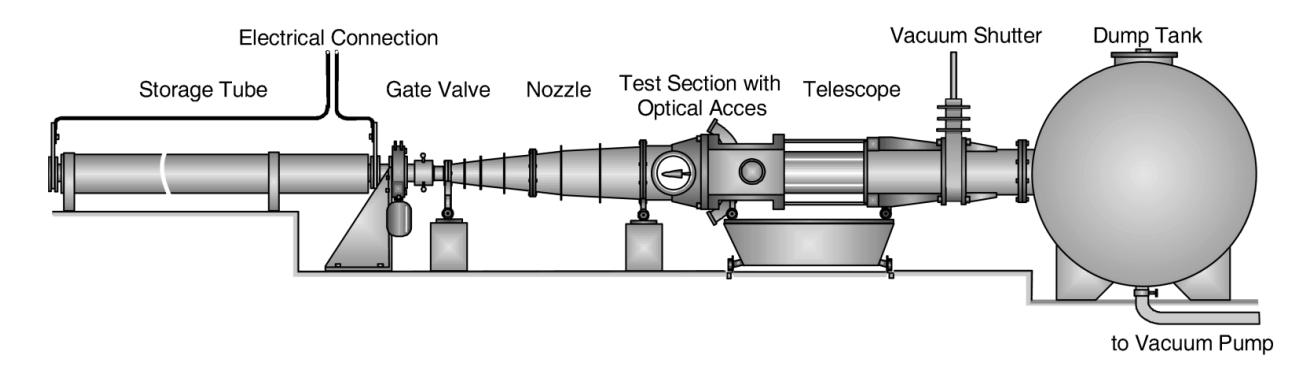


Figure 2: Sketch of the Ludwieg-Tube Facility at DLR Göttingen.

Tube A Α A В В В Ma 2 6.85 5 6  $p_0$ , MPa 0.05 - 0.70.06 - 0.60.08 - 1.00.4 - 2.90.4 - 3.40.4 - 3.6 $T_0, K$ 236-262 241-267 340-610 258-287 410-640 440-655  $Re_{1,\infty}$ ,  $10^6 \,\mathrm{m}^{-1}$ 10-110 6-70 4-60 5-55 3-28 2-17 Test section  $0.34 \times 0.35 \,\mathrm{m}^2$  $0.5 \times 0.5 \,\mathrm{m}^2$  $0.5 \times 0.5 \,\mathrm{m}^2$ ø0.5 m ø0.5 m ø0.5 m

Table 1: Flow parameter range of the RWG

length, with a width that tapers from 300 mm at the leading edge to 180 mm at the rear. To document the shape of the leading edge, an imprint was made in lead after the measurements. The lead imprint was optically measured using a Keyence profilometer VR-5000 and corresponds to a blunt leading edge with a edge thickness of  $270 \,\mu m$ . The shape of the concave bump was the same as in Schülein et al.<sup>9</sup> and the generalised local wall angle on the windward side of the bump is defined by

$$\frac{\theta}{\theta_{\text{max}}} = 1.69 \left(\frac{\tilde{x}}{L}\right)^2 - .69 \left(\frac{\tilde{x}}{L}\right)^3 \quad \text{for} \quad 0 \le \tilde{x}/L < 1.$$
 (1)

The maximum wall angle was  $\theta_{\text{max}} = 12^{\circ}$  and the half length of the bump was L = 30 mm. The shape of the bump was mirrored at the crest position of  $x_{\text{crest}} = 280$  mm. Along the symmetry plane, wall pressure taps with 0.3 mm diameter were drilled at the positions  $x_i = 198.75$  mm +  $i \cdot 2.5$  mm for  $i \in \{1, 2, ..., 55\}$ . The static wall pressures were recorded with two 32-port miniature electronic differential pressure measurement module with a measurement range of  $\pm 15$  psi from PSI in conjunction with a DTC Initium system at a sampling rate of 650 Hz. The wedge-shaped shock generator, with a width of 200 mm, is positioned 200 mm downstream of the plate leading edge and measures 70.6 mm in length. It generates a flow deflection of  $12^{\circ}$  and its height towards the flat plate can be adjusted in increments of 0.1 mm to vary the shock impingement position.

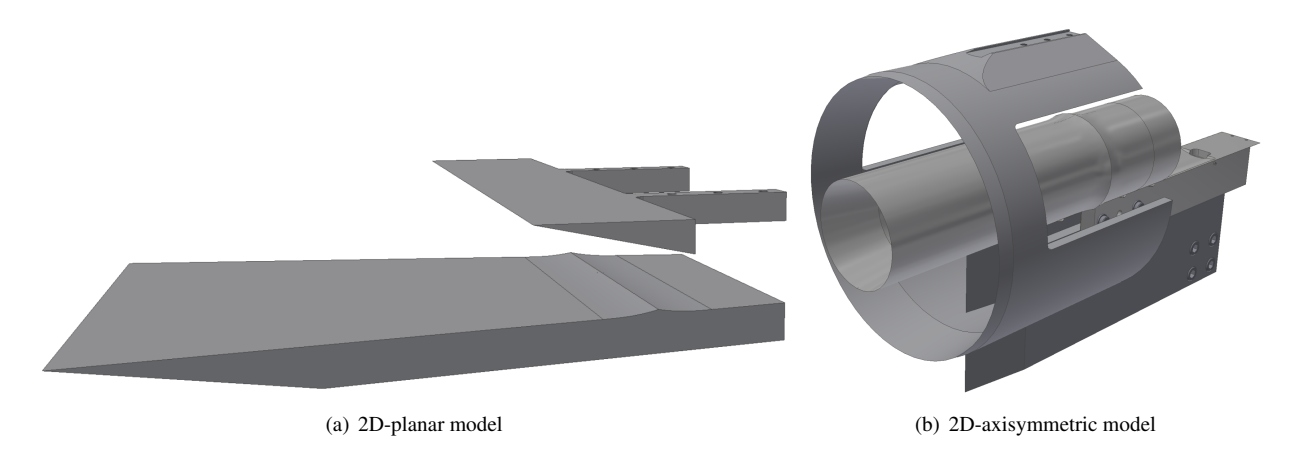


Figure 3: Canonic models for validating the concave bump concept.

The axisymmetric model is a hollow cylinder with an outer radius of 50 mm and a length of 400 mm. The

evaluation of the leading edge yielded a rounded shape with a radius of  $10 \,\mu\text{m}$ . The axisymmetric model uses the identical shape of the concave bump and the crest position is again at  $x_{\text{crest}} = 280 \,\text{mm}$ . The hollow cylinder is equipped with 32 wall pressure taps at  $x_i = 247 \,\text{mm} + i \cdot 2 \,\text{mm}$  for  $i \in \{1, 2, ..., 32\}$ , which were connected to one 32-port PSI module with a measurement range of  $\pm 5 \,\text{psi}$  to improve the accuracy. The sampling rate was again 650 Hz. The axisymmetric shock generator had a radial distance to the symmetry axis of 130 mm at the leading edge and enforces a flow deflection of  $8.35^{\circ}$  over a length of  $54.5 \,\text{mm}$ . In the axisymmetric flow situation, the deflection induced by the generated shock amplifies towards the symmetry axis, whereby the rate of amplification depends on the Mach number. The deflection angle of the shock generator was optimized for the Ma = 3 conditions to align the flow deflection at the bump crest with the local bump angle. The shock generator has cut outs on both sides to provide optical access to the SWBLI for shadograph images. The hollow cylinder was mounted on a carriage and could be moved in streamwise direction to vary the shock impingement position.

# 3. Numerical setup

The numerical simulations were conducted by the DLR finite volume flow solver TAU. <sup>10</sup> TAU solves the compressible Reynolds-averaged Navier-Stokes-equations (RANS) on hybrid structured/unstructured grids. The equations were spatially discretised by a second order upwind method with the flux splitting scheme AUSMDV<sup>12</sup> and the steady RANS simulations were converged by a backward Euler time stepping method. The numeric transition onset location of the boundary layer was set manually to x = 55 mm. Schülein et al. <sup>9</sup> performed a grid convergence study for the 2D-planar concave bump at the Ma = 3 conditions at the RWG, which indicated an adequate convergence for grid sizes with  $\approx 480\,000$  nodes, which were used in the current study. Table 2 summarizes the simulated freestream conditions for the concave bump models.

Table 2: Experimental investigated and simulated RWG freestream conditions

Ма	$Re_{1,\infty}$	$p_{\infty}$	$T_{\infty}$
3	$26 \cdot 10^6  \text{m}^{-1}$	7315 Pa	90 K
5	$26 \cdot 10^6  \text{m}^{-1}$	2950 Pa	70 K

## 3.1 Choice of the turbulence model

To select the appropriate turbulence model, the boundary layer Pitot-tube measurements conducted by Touré<sup>11</sup> on a flat plate at the RWG Ma=3 and  $Re_{1,\infty}=46\cdot 10^6\,\mathrm{m}^{-1}$  conditions were used as the benchmark. The numerical replication of the Pitot-tube measurements were performed with three models for the Reynolds stresses, which were the explicit algebraic Reynolds stress model (EARSM) of Hellsten,<sup>2</sup> the Menter shear stress transport k- $\omega$  turbulence model (Menter SST)<sup>5</sup> and the Wilcox k- $\omega$  model.<sup>13</sup> Figure 4 compares the Ma profiles of the three Reynolds stress models with the experimental results at the location  $x=153\,\mathrm{mm}$ . The profiles were scaled by the conditions at the boundary layer edge  $\delta$ .

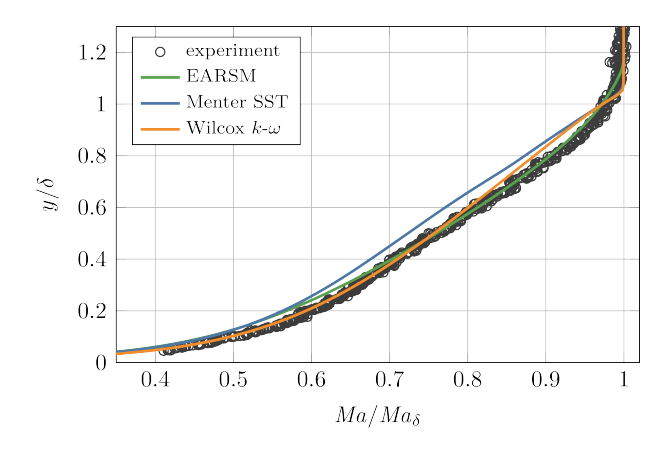


Figure 4: Influence of the turbulence model on the numerical Ma profiles at an undisturbed plate at x = 153 mm.

The Wilcox k- $\omega$  model reproduces the experimental data significantly better in the lower half of the boundary

layer than in the upper half. In contrast, the EARSM model exhibits the opposite behaviour. The Menter SST model deviates the most from the experimental Ma profile and seems to be unsuited for the current application. Initial simulations showed that the EARSM model exhibited superior agreement with experimental data for larger separation bubbles, while the Wilcox k- $\omega$  model demonstrated better accuracy in predicting smaller separation bubbles. The observations from the boundary layer profile comparison can aid in interpreting the numerical reproduction of separation bubbles. The analysis suggests that predicting small separation bubbles requires accurate reproduction of the near-wall region of the boundary layer, whereas replicating large separations depends critically on the proper representation of the Reynolds stresses in the upper boundary layer half to calculate the momentum exchange across the dividing streamline. Since none of the tested turbulence models can accurately predict the Ma distribution across the entire boundary layer profile, the choice of turbulence model must prioritize the specific flow characteristic that requires the highest fidelity in simulation. Given that the concave bump concept relies on suppressing the separation bubble at the design point, the Wilcox k- $\omega$  model was selected as the most suitable choice for replicating the flow field numerically.

#### 4. Results and Discussion

## 4.1 Validation of the bump concept

The shadowgrams in Fig. 5 exemplify, for the planar plate model at Mach 3, how the flow topology of the SWBLI and the separation bubble changes when the impinging shock hits the windward side ( $x_{imp} = 282.9 \text{ mm}$ ), the leeward side ( $x_{imp} = 293.4 \text{ mm}$ ), or the crest of the concave bump ( $x_{imp} = 288.1 \text{ mm}$ ). To quantify the shock impingement location  $x_{imp}$ , an edge detection and the Hough transformation were utilized to determine the spatial orientation of the shock and its virtual intersection point with the abscissa of the coordinate system.

When the impinging shock interacts with the concave bump at its design point, the SWBLI is successfully transformed into a separation free interaction and the measured wall pressure distribution  $p/p_1$  matches the conceptually anticipated uniform increase. The alignment of experimental results with theoretical predictions validates the concave bump concept experimentally. The measured wall pressure  $p_1$  in the undisturbed region of the boundary layer was used to normalize the data of the respective measurement.

If the design point is missed, the concave bump fails to fully suppress the separation bubble. On the windward side, even minor deviations of  $x_{\rm imp}$  from the design point lead to the formation of relatively large separation bubbles. This occurs because the boundary layer now experiences both the adverse pressure gradient induced by the compression waves generated by the bump and the shock induced pressure rise. On the leeward side the separation bubble size scales slower with the distance of  $x_{\rm imp}$  to the crest, because the crest fixates the separation point and limits the upstream influence. The distinct flow behaviour, observed on the windward and leeward sides of the bump, suggests that the efficiency enhancement achieved through the concave bump is asymmetric with respect to the relative position of  $x_{\rm imp}$  to the bump crest.

The wall pressure distributions obtained from the CFD simulations were compared with the experimental data. For both off-design locations, the CFD simulations were unable to accurately replicate the wall pressure measurements. This discrepancy is attributed to the Wilcox model's inadequate reproduction of the *Ma* profiles in the outer part of the boundary layer (see section 3.1). As already mentioned, the replication of the outer part of the boundary layer profile becomes relevant for large separation bubbles, as it determines the momentum transfer across the dividing streamline of the separation bubble. At the design point, the wall pressure distributions exhibit a better agreement, because the Wilcox model accurately resolves the near-wall region of the boundary layer, which is crucial in determining the onset of separation.

#### 4.2 Numeric quantification of advantages by the bump

After the experimental validation that the concave bump can suppress the flow separation at SWBLI and the sufficient numerical replication of the flow situation, the efficiency advantages of the bump will be quantified. To analyse the total pressure recovery downstream of the SWBLI, a virtual flow channel was investigated, by calculating the path of a streamline through the interaction region of the SWBLI. The starting point was chosen at (x, y) = (200 mm, 12.5 mm) and the path of the streamline is depicted in Fig. 11 by the red line.

The compression caused by the impinging shock is evident from the reduced wall distance of the streamline downstream of the SWBLI. Further downstream the height of the streamline  $n_s$  increases again due to the expansion fan originating from the rear of the shock generator and the displacement effect of the growing boundary layer. By definition, no mass transfer exists perpendicular to the streamline, so it is sufficient to consider any position downstream of the SWBLI in order to study the potential total pressure recovery. For the 2D-planar model, the total pressure profiles

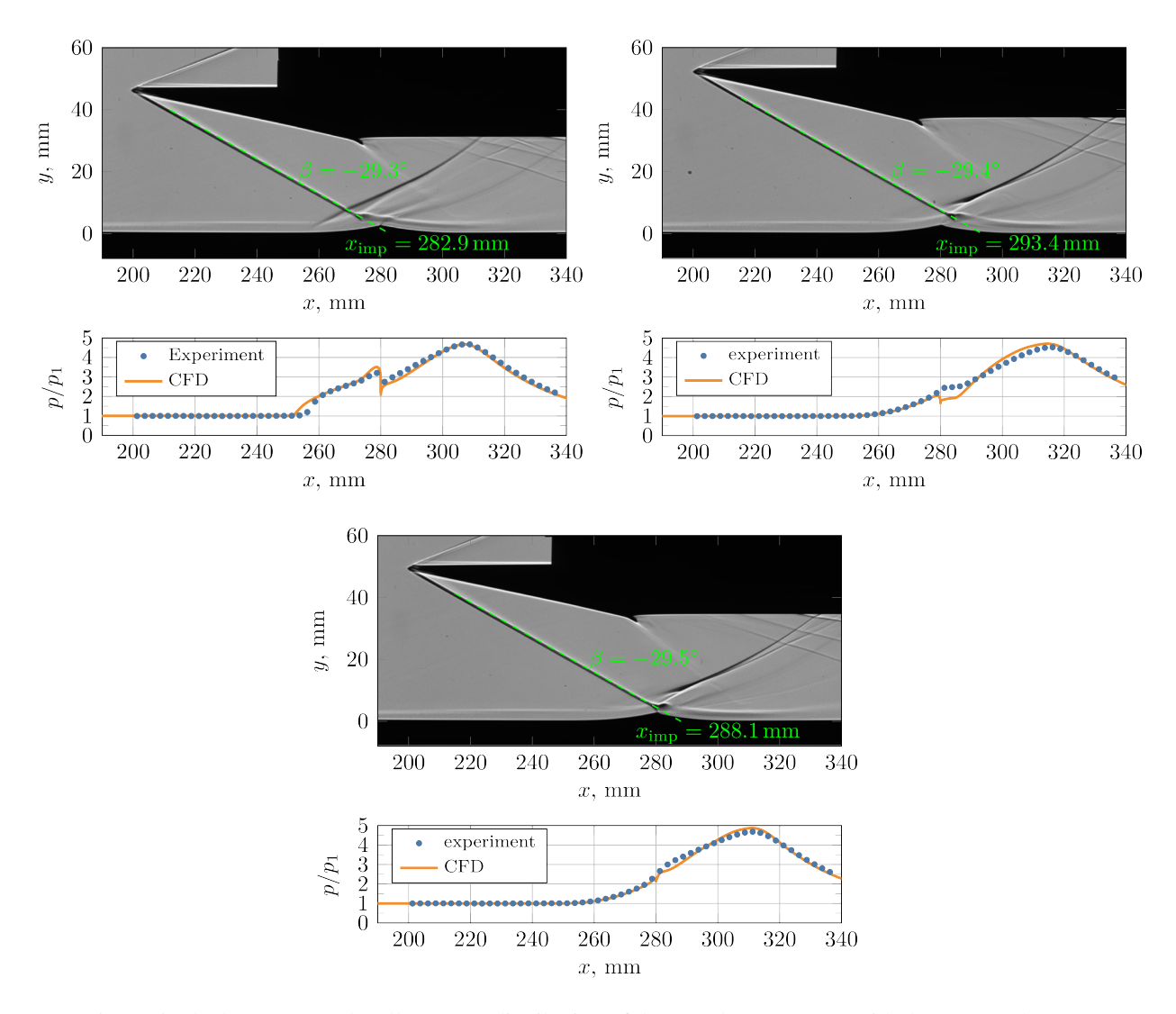


Figure 5: Shadowgrams and wall pressure distribution of the 2D-planar SWBLI with the concave bump.

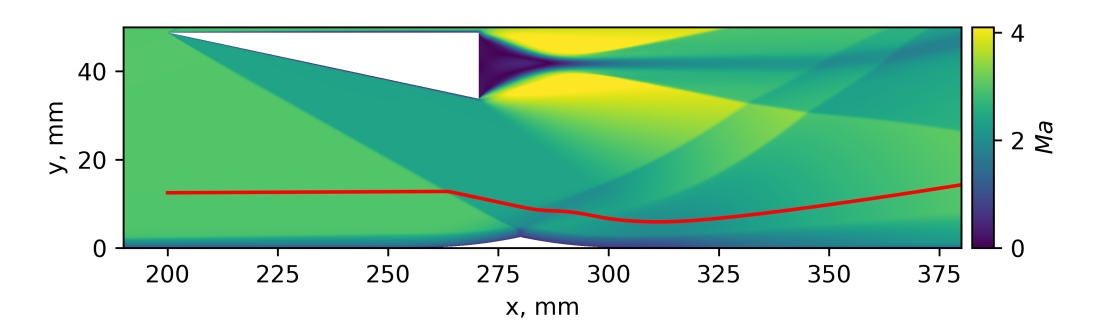


Figure 6: Streamline path through the interaction region of a SWBLI with bump.

up to the local streamline height were analysed at the streamwise position x = 375 mm. The investigated total pressure profiles are scaled by the total pressure of the inflow  $p_{\text{tot},\infty}$  and are plotted in Fig. 7 for the cases with and without the bump at  $x_{\text{imp}} = 285.5$  mm. The light blue area highlights, that with the bump the total pressure close to the wall is increased compared to the reference case, which means that the boundary layer is more resistant to adverse pressure gradients further downstream. A further advantage of the modified total pressure profile is the more efficient compression of the fluid, which leads to a smaller streamline height. The total pressure value at the streamline height is also higher with the implemented bump, which means the total pressure losses caused by the SWBLI were reduced.

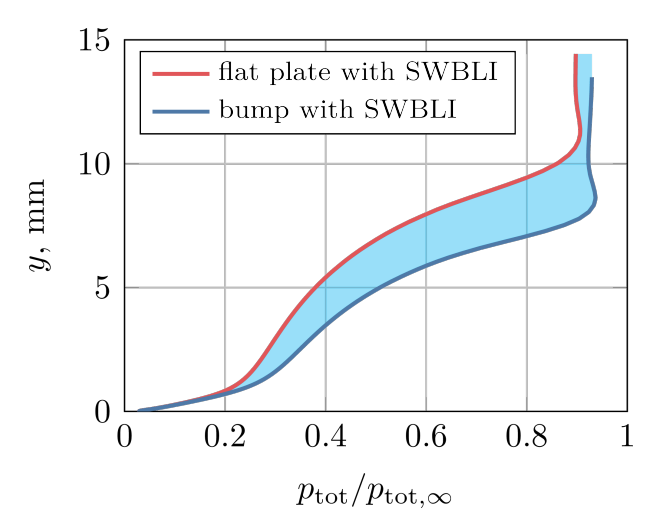


Figure 7: profiles of the total pressure at x = 375 mm for  $x_{imp} = 285.5$  mm with and without the bump.

While the bump performs well at the design point, the off-design situation was investigated as follows. The average total pressure at a cross section of the virtual flow channel

$$\frac{\bar{p}_{\text{tot}}}{p_{\text{tot},\infty}} = \int_0^{n_s} \frac{p_{\text{tot}}}{n_s p_{\text{tot},\infty}} \bigg|_{x=375 \text{ mm}} dn$$
 (2)

was calculated for various  $x_{\rm imp}$  and is plotted in Fig. 8. The values indicate the remaining total pressure inside the virtual flow channel at the evaluation position. To indicate the  $p_{\rm tot}$  losses due to dissipation effects of the boundary layer itself, the same analysis was also conducted for a flat plate without a SWBLI and these losses are visualised by the red crosshatched area. The remaining total pressure on the flat plate with SWBLI is about  $\bar{p}_{\rm tot}/p_{\rm tot,\infty}=0.57$  and varies only marginally with the investigated  $x_{\rm imp}$ , since the boundary layer in this region remains largely unchanged. With the bump, the average total pressure of the flow channel has a local maximum, which corresponds to the design point. As the maximum ( $\bar{p}_{\rm tot}/p_{\rm tot,\infty}=0.66$ ) lies midway between the SWBLI without the bump and the  $p_{\rm tot}$  losses of the undisturbed boundary layer, the shock induced  $p_{\rm tot}$  losses are halved by the bump. Considering that the bump only affects the SWBLI region with the reflected shocks and not the impinging shock itself, it seems that the potential benefit of the bump is completely realized.

In the off-design the benefit of the bump declines smoothly and further away the effect of the bump is even detrimental. Since the bump's effectiveness is not highly sensitive to the precise alignment of the impinging shock with its crest, its application is significantly simplified.

#### 4.3 The axisymmetric application of the bump

The second canonic wind tunnel model serves the purpose to validate that the concave bump can also be used in axially symmetric configurations to prevent flow separation at SWBLI. Figure 9 shows the shadowgrams and the measured wall pressure distributions of the axisymmetric model for the freestream Ma of 3 as well as 5 in the situation where the impinging shock hits the crest of the bump.

At both Ma, the identical concave bump can suppress the flow separation of the SWBLI. As expected, the wall pressure distribution increases evenly over the SWBLI, with the exception of one data point. The deviating data point is located directly downstream of the crest. After a more detailed examination, the reason appears to stem from an insufficiently long shock generator. The Prandtl-Meyer expansion fan, originating at the rear of the shock generator, interacts with the generated shock before the shock impinges on the bump and reduces the pressure rise over the SWBLI. As a consequence the flow is overexpanded at the crest and the first wall pressure point behind the crest is

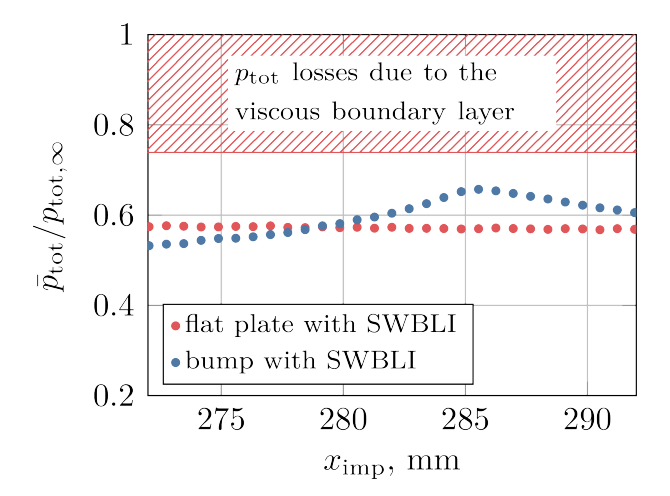


Figure 8: Averaged total pressure recovery at different shock impingement positions for the planar model at Ma = 3.

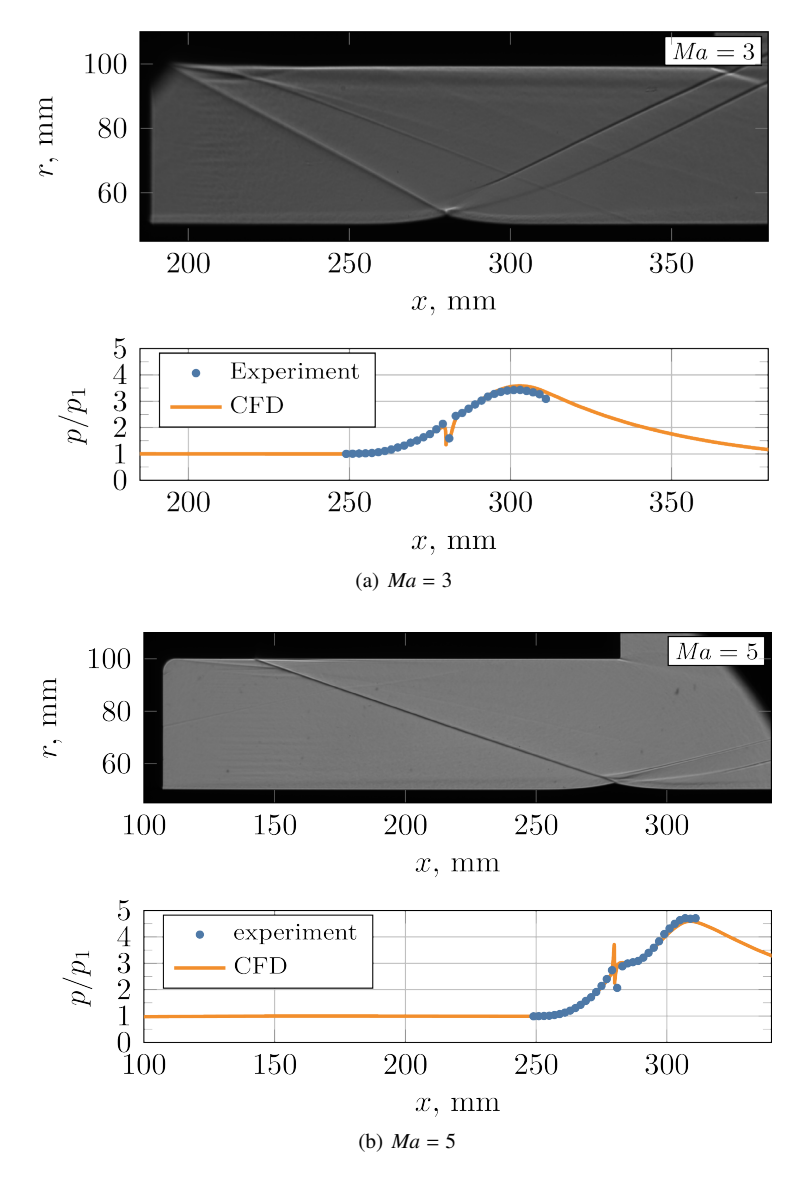


Figure 9: Shadowgrams and wall pressure distribution of the 2D-axisymmetric SWBLI with the concave bump.

reduced. This deviation can easily be overcome in the design of future models. The TAU simulations reproduced the outlier in the wall pressure distribution, because the identical model geometry was simulated.

To analyse the benefits of the bump in the axisymmetric case regarding the total pressure recovery, the mean total pressure was again determined by using a virtual channel. Due to the geometric boundary conditions in the axisymmetric case, the starting point of the streamline was at (x, r) = (125 mm, 62 mm) and the mean total pressure was evaluated at x = 350 mm. The results are shown for various  $x_{\text{imp}}$  in Fig. 10 for the two Mach numbers.

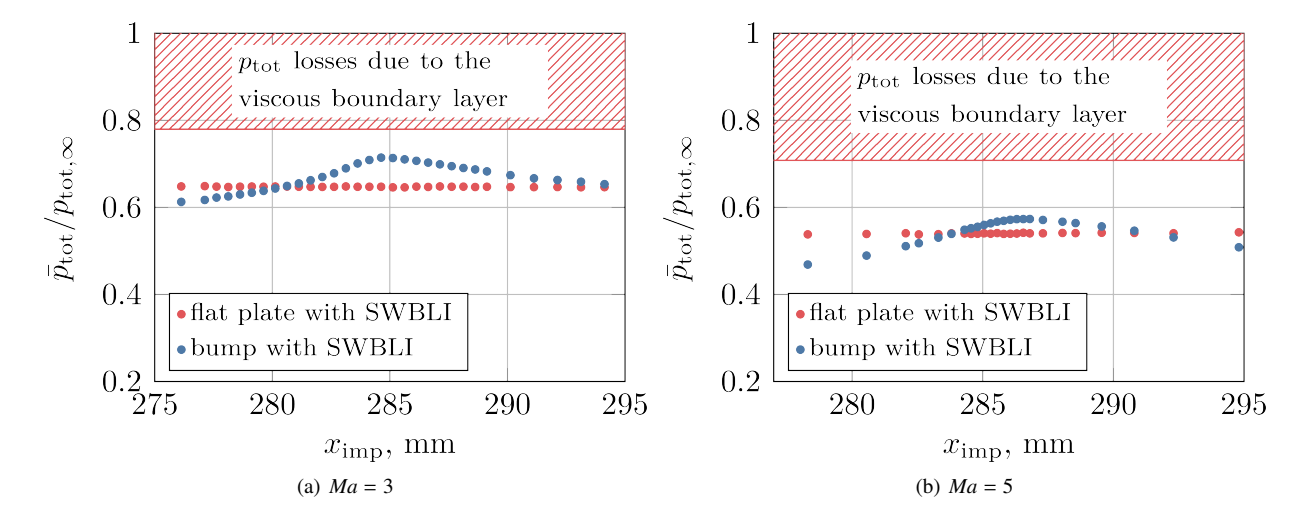


Figure 10: Averaged total pressure recovery at different shock impingement positions for the axisymmetric model.

At both Ma, the concave bump leads to a local maximum in  $\bar{p}_{\text{tot}}/p_{\text{tot},\infty}$  at the design point that is above the reference configuration without the bump. Existing scaling laws<sup>6</sup> indicate an inverse behaviour between the length of separation bubbles and Ma. Small separation bubbles offer little potential for the optimization through the bump, so the realized benefit in the Ma = 5 case is lower. A contributing factor to the lower performance in the Ma = 5 case may stem from the optimization of the shock generator deflection angle for Ma = 3. At Ma = 5, the non-ideal deflection leads to an excessive compression of the flow on the windward side of the bump and an over-expansion at the bump crest. These dispensable pressure changes are not conducive for efficiency.

#### 4.4 The bump on truncated 2D Prandtl-Meyer inlets

With the successful validation of the bump concept on canonical wind tunnel models, the benefits of a separation free SWBLI with an enhanced flow compression by the concave bump for more realistic inlet configurations will be demonstrated. For the demonstration a family of truncated 2D Prandtl-Meyer inlets, which differed primarily in their total contraction, were generated and investigated numerically. The geometry parameters were either fixed, like the height between the leading edge and the cowl lip  $h_{\rm LE}$ , or expressed as a dependency of the leading edge ramp angle. As a consequence, the parameter study regarding the total inlet contraction  $h_{\rm LE}/h_{\rm min}$  can be conducted by varying only the leading edge ramp angle, whereby  $h_{\rm min}$  the minimal height of the inlet duct describes. Additionally, a concave bump could be added for the cowl induced SWBLI. Examples for the generated inlets are shown in Fig. 11.

The simulations were conducted with the Ma = 5 freestream conditions listed in table 2 and the boundary layer was assumed to be fully turbulent. The computational domain of the inlet ends at the plane between the isolator and the combustion chamber. To ease the starting process of the simulation the boundary condition at the exit plane was set to 1 Pa.

For the reference case without the concave bump the total contraction could be increased till a value of 7.44. Beyond this point the inlet did not start, most likely because the shock induced separation bubble leads to an effective contraction of the inlet cross-sectional area above the critical level. With the enhanced flow compression in a separation free SWBLI due to the concave bump, the limit for the total contraction could be exceeded up to 10.4.

To highlight the advantage of an increased inlet contraction on the pressure recovery, the back pressure at the exit boundary condition of the inlet was gradually increased until the inlet blocked. Figure 11 shows the *Ma* distributions for the maximum back pressure before the inlet unstarts in the respective case. The back pressure leads to a shock train<sup>4</sup> near the throat that decelerates the flow to subsonic velocities at the expense of severe total pressure losses due to the strong shocks involved. In the case with the bump, the Mach number at the smallest cross-section is lower due to the higher contraction and as a consequence the total pressure losses of the shock train are reduced, leading to the

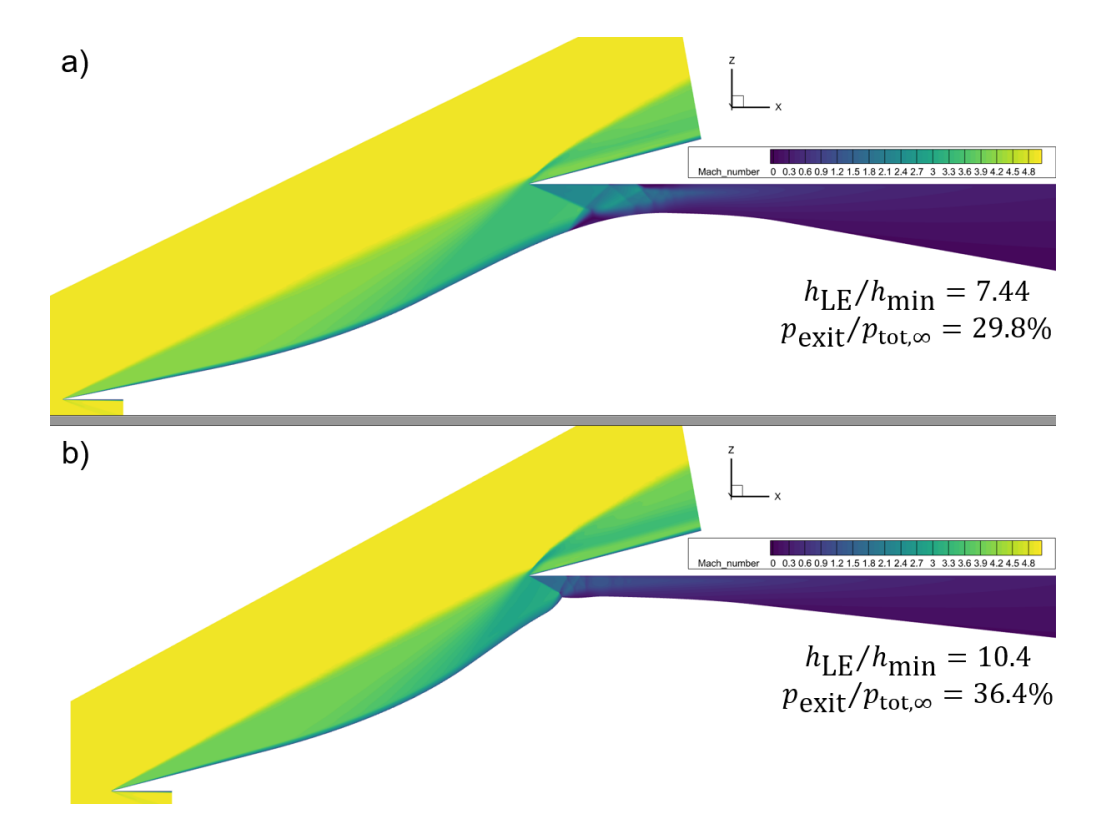


Figure 11: Ma distributions for the maximum contraction of the Prandtl-Meyer inlets without (a) and with (b) the bump.

increased maximum back pressure of the combustion chamber. At higher pressure, the combustion chamber can be built more compact and the free path length of the molecules is reduced, which benefits chemical combustion.

# 5. Conclusion

The concave bump concept, a passive flow control element for modifying impinging SWBLI to separation free interactions, was validated experimentally on two canonical wind tunnel models. The 2D-planar and 2D-axisymmetric impinging SWBLI test models enabled the systematic variation of the shock impingement location to evaluate the behaviour of the bump at the design point and in the off-design. In the design point, no separation bubble was visible in the shadowgrams of the flow. The measured wall pressure distributions aligned with the theoretical expectations for an interaction without separation, demonstrating the capability of the concave bump to suppress it.

Accompanying RANS simulations could be validated by comparing the wall pressure distributions to the experiments, which enabled the more detailed investigation of performance gains through the use of the bump. The analysis of a virtual channel through the SWBLI revealed a more effective compression of the flow with an increased pressure recovery by using the bump. Losses in total pressure due to the impinging shock were halved at the design point. If the impinging shock misses the crest of the bump, the performance gains are initially reduced and eventually, the bump becomes detrimental. The beneficial range of the investigated bump covered several millimetres of  $x_{\rm imp}$ .

A separate numerical study on truncated 2D Prandtl-Meyer inlets was conducted to demonstrate the benefits of the more efficient compression achieved by the concave bump in an application oriented scenario. The concave bump enabled larger total contraction ratios, which also resulted in a higher maximum combustion chamber pressure and therefore increasing the overall efficiency of the inlet.

While the concave bump effectively suppressed flow separation on canonical 2D impinging SWBLI geometries, its applicability to 3D flow configurations remains to be demonstrated.

# 6. Acknowledgments

This work was supported by Basic Funding from the German MoD (BMVg). The authors are grateful for the technical and experimental assistance from the RWG staff.

#### References

- [1] P. Gruhn and A. Gülhan. Experimental investigation of a hypersonic inlet with and without sidewall compression. *Journal of Propulsion and Power*, 27(3):718–729, 2011.
- [2] A. Hellsten. *New two-equation turbulence model for aerodynamics applications*. PhD thesis, Helsinki University of Technology, Laboratory of Aerodynamics, Finnland, 2004.
- [3] D. Herrmann, S. Blem, and A. Gülhan. Experimental study of boundary-layer bleed impact on ramjet inlet performance. *Journal of Propulsion and Power*, 27(6):1186–1195, November 2011.
- [4] K. Matsuo, Y. Miyazato, and H.-D. Kim. Shock train and pseudo-shock phenomena in internal gas flows. *Progress in Aerospace Sciences*, 35(1):33–100, January 1999.
- [5] F. R. Menter. Two-equation eddy-viscosity turbulence models for engineering applications. *AIAA journal*, 32(8):1598–1605, 1994.
- [6] D. Needham and J. Stollery. Boundary layer separation in hypersonic flow. *AIAA 1966-455, 4th Aerospace Sciences Meeting*, 1966.
- [7] H. H. Pearcey. *Boundary layer and flow control*, volume 2, chapter Introduction to shock-induced separation and its prevention by design and boundary layer control, pages 1166–1344. Pergamon Press, 1961.
- [8] E. Schülein. Skin friction and heat flux measurements in shock/boundary layer interaction flows. *AIAA Journal*, 44(8):1732–1741, 2006.
- [9] E. Schülein, C. Schnepf, and S. Weiss. Concave bump for impinging-shock control in supersonic flows. *AIAA Journal*, 60(5):2749–2766, May 2022.
- [10] D. Schwamborn, T. Gerhold, and R. Heinrich. The DLR TAU-code: Recent applications in research and industry. In *ECCOMAS CFD 2006: Proceedings of the European Conference on Computational Fluid Dynamics*. Delft University of Technology, 2006.
- [11] P. S. R. Touré. *Turbulente Stoß-Grenzschicht-Wechselwirkungen durch laufende Verdichtungsstöße*. PhD thesis, Technical University of Braunschweig, 2022.
- [12] Y. Wada and M.-S. Liou. A flux splitting scheme with high-resolution and robustness for discontinuities. In *32nd Aerospace Sciences Meeting and Exhibit*, page 83, 1994.
- [13] D. C. Wilcox. Reassessment of the scale-determining equation for advanced turbulence models. *AIAA journal*, 26(11):1299–1310, 1988.